JPhys Materials

PAPER • **OPEN ACCESS**

Formation and corrosion-protective performance of zirconium conversion coating on aluminium heat exchanger components

To cite this article: Ana Kraš *et al* 2026 *J. Phys. Mater.* **9** 035006

Journal of Physics: Materials

OPEN ACCESS

RECEIVED
14 March 2026

REVISED
10 June 2026

ACCEPTED FOR PUBLICATION
23 June 2026

PUBLISHED
10 July 2026

PAPER

Formation and corrosion-protective performance of zirconium conversion coating on aluminium heat exchanger components

Ana Kraš[1], Barbara Kapun[1,2], Nina Kovač[1,2], Matejka Podlogar[3], Sašo Šturm[3], Ingrid Milošev[1], Marko Kralj[4] and Peter Rodič[1,*]

[1] Department of Physical and Organic Chemistry, Jožef Stefan Institute, Jamova c. 39, 1000 Ljubljana, Slovenia
[2] Jožef Stefan International Postgraduate School, Jamova c. 39, 1000 Ljubljana, Slovenia
[3] Department for Nanostructured Materials, Jožef Stefan Institute, Jamova c. 39, 1000 Ljubljana, Slovenia
[4] Gorenje d.o.o., Hisense Europe, Partizanska c. 12, 3320 Velenje, Slovenia
[*] Author to whom any correspondence should be addressed.

E-mail: peter.rodic@ijs.si

Keywords: heat exchanger, aluminium, surface treatment, corrosion protection, zirconium conversion coating

Supplementary material for this article is available online

Abstract

This study investigates the corrosion protection of aluminium heat exchangers used in freezers with a zirconium conversion coating (ZrCC). Tube and fins sections were subjected to a three-step surface treatment comprising (i) alkaline cleaning, (ii) acid desmutting, both with commercial SurTec® products, and (iii) deposition of conversion of Zr coating in a hexafluorozirconic acid (H_2ZrF_6) bath. The resulting surfaces were characterised for morphology, composition, and corrosion behaviour using scanning electron microscopy with energy-dispersive x-ray spectroscopy, x-ray photoelectron spectroscopy, potentiodynamic polarisation, and neutral salt spray (NSS) testing. Zr formed a ∼70 nm oxide–hydroxide layer that preferentially nucleated and grew on cathodic Fe-containing intermetallic particles in tubes and fins. The coating improved passivity and delayed pit initiation in chloride-containing environments by broadening the passivity span ΔE up to 500 mV. Accelerated corrosion testing in NSS (ASTM B117) demonstrates that ZrCC can provide efficient protection for up to 90 h on tube-and-fin substrates, thereby supporting their implementation in industrial heat-exchanger production.

1. Introduction

Heat exchangers are essential components in refrigeration, air-conditioning, and process-cooling systems, where reliable performance in a relevant environment and long life without maintenance are crucial [1]. These components are manufactured from aluminium and its alloys due to their high thermal conductivity, low density, good formability, and favourable cost/performance ratio [2–5]. In aluminium fin–tube heat exchangers, thin fins are joined to tubes, forming high-surface-area channels that enable efficient heat transfer either releasing heat or absorbing heat from the surrounding environment. However, industrial trends toward thinner fins, changing working conditions, higher fin densities, and increasingly complex louvred geometries have simultaneously increased susceptibility to corrosion under service conditions [6]. Experimental studies have shown that ice formation [7–9] and corrosion-induced fin thinning or flow blockage can significantly impair heat-transfer efficiency [10].

The operating environments of heat exchangers further exacerbate this vulnerability. Cyclic humidity and temperature fluctuations, atmospheric chlorides, condensate formation, and the presence of brazed joints create pronounced chemical and electrochemical heterogeneity. As a result, localised corrosion processes (including pitting, crevice corrosion, and galvanic corrosion at brazed regions) are the dominant degradation mechanisms in aluminium heat exchangers [11, 12]. Although all-aluminium designs are often assumed to mitigate galvanic effects compared with systems employing dissimilar metals, practical experience shows that such assemblies remain highly susceptible to corrosion, the deposition of white aluminium oxide or hydroxide corrosion products, and fouling [11].

Fins are particularly vulnerable owing to their minimal thickness, large wetted surface area, and direct exposure to condensate. Consequently, heat-exchanger designs often deliberately select fins that are more anodic than the tube alloys, allowing them to act sacrificially and thereby delaying perforation as tube gauges decrease [12,]. This design philosophy imposes stringent requirements on surface treatments: coatings must be extremely thin, thermally benign, and chemically robust. Conventional fin stock, typically based on wrought aluminium alloys series 1xxx, 3xxx, or 8xxx, provides good formability and moderate corrosion resistance, but additional protection is often required [13–16]. In this context, inorganic conversion coatings such as zirconium-based conversion coatings (ZrCC) [17–19] offer clear advantages over organic or hybrid systems which may introduce thermal resistance or degrade under cyclic wet–dry exposure [20].

ZrCCs are therefore attractive candidates for protecting aluminium heat-exchanger components. They form thin (typically 10–80 nm), adherent, largely amorphous Zr(IV) (hydr)oxide layers, whose morphology and thickness are governed by bath pH, zirconium concentration, immersion time, temperature, and ageing [19, 21–23]. Deposition preferentially occurs above cathodic intermetallic particles (IMPs), reflecting the strong influence of local electrochemical activity on coating formation [19]. Numerous studies have demonstrated that such coatings significantly reduce corrosion in chloride-containing electrolytes [18, 21–24].

Moreover, they have been shown to perform effectively on low-alloyed wrought aluminium, particularly when combined with organic topcoats [21, 25]. Industrial patents [26, 27] and technical sources further describe the use of zirconium-containing pretreatments in all-aluminium heat exchangers, commonly as a precursor to hydrophilic or organic coatings [28–30], highlighting their technological relevance. Furthermore, owing to their nanometric thickness, ZrCCs do not measurably impair heat transfer while still enhancing corrosion resistance. This combination makes them particularly attractive for fin–tube heat exchangers; however, systematic investigations of ZrCC formation mechanisms and long-term performance in such complex geometries remain scarce.

Although long-term industrial implementations may integrate ZrCCs with additional topcoats, the present work focuses on the intrinsic behaviour and protective effectiveness of the zirconium conversion layer itself. In our earlier work [31], response surface methodology was used to optimise ZrCC processing on another serial of aluminium alloy AA5754 (where 2.6–3.6 wt.% of magnesium is present as major alloying element and other elements such as Mn 0.5, and Fe 0.4 wt.%), revealing that microgalvanic coupling between IMPs and the aluminium matrix plays a key role in controlling coating deposition kinetics. The corrosion resistance of heat exchanger materials and protective systems is commonly evaluated using accelerated laboratory tests, such as neutral salt spray (NSS), to predict field performance [16].

The present study extends the corrosion investigation from fundamental heat-exchanger components by comparing the separately tested tube and fin substrates to an industrial aluminium heat exchanger (aluminium 1050). The aim is to assess how alloy composition, microstructure, and surface condition influence ZrCC formation and corrosion response, and to determine whether optimised ZrCC conditions to be transferred to a heat exchanger with complex geometries for practical applications (to be developed for another series despite AA5754 [31]). By directly comparing both tube and fin substrates, this work provides better insight into the suitability of Zr-based conversion coatings. In addition, further testing of aluminium heat exchangers (combined tube-and-fin) identifies the microstructural factors governing their formation and corrosion-protective performance, and these are also tested under accelerated conditions using NSS.

2. Methods

2.1. Samples and solution preparation

Heat exchanger samples of the commercial pure aluminium 1050 (with Al purity >99.5%) were provided by Hisense Europe (Gorenje d.o.o., Slovenia) and consisted of aluminium tube-and-fin segments (figure 1(a)).

The tube and fin surfaces were used as-received, without any mechanical surface pretreatment. The heat exchanger was cut into smaller pieces (figures 1(b) and (c)). After surface preparation, the samples were ultrasonically cleaned in absolute ethanol (37 kHz, 100% power) for 5 min using an Elmasonic P bath (Elma Schmidbauer GmbH, Germany), rinsed with ethanol and Milli-Q (deionised) water, and dried with compressed nitrogen.

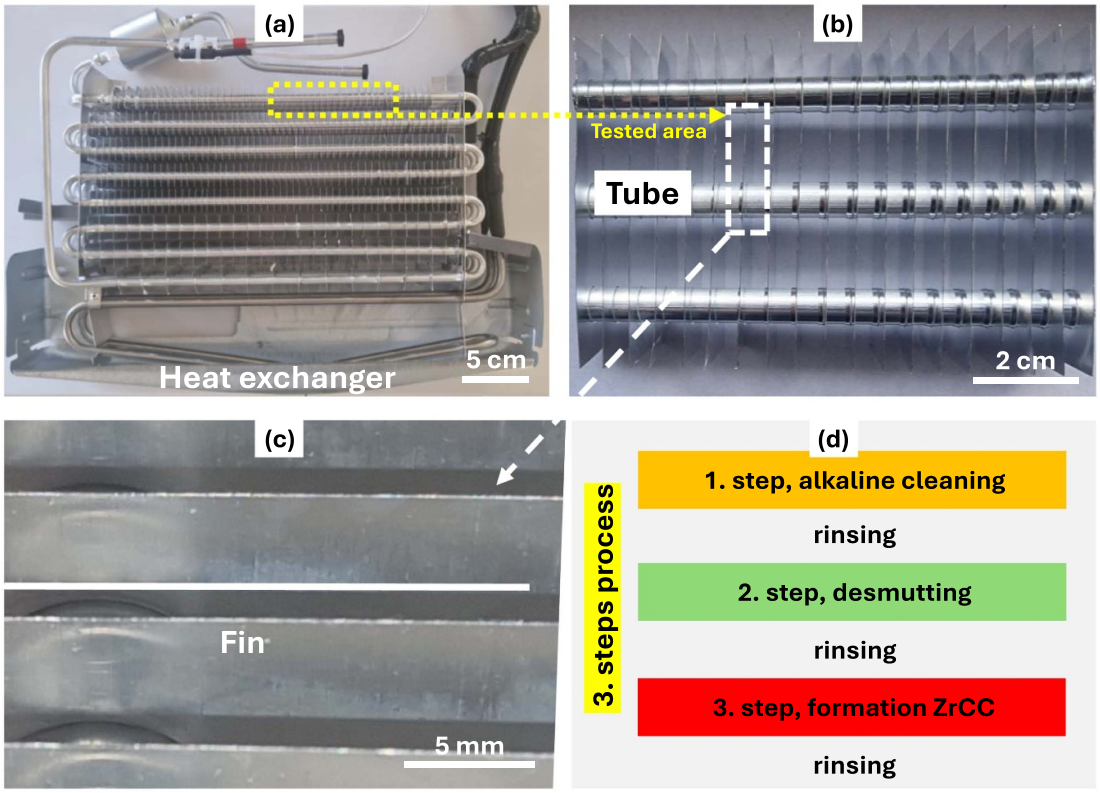

Figure 1. (a) Freezer heat exchanger and (b), (c) magnified views of the tested areas on the heat-exchanger tubes. (d) Schematic overview of the three-step zirconium conversion coating (ZrCC) formation process, including rinsing with distilled water after each step.

2.2. Reagents for alkaline cleaning, desmutting and ZrCC formation

All solutions were prepared using analytical reagent-grade chemicals in their as-received state. Absolute ethanol (EtOH, Merck KGaA, Darmstadt, Germany) was used for cleaning and rinsing; NaCl (Fisher Scientific, Leicestershire, UK) for electrochemical testing, NH_4HCO_3 (Sigma-Aldrich, Steinheim, Germany), and H_2ZrF_6 (50 wt. % in H_2O, Sigma-Aldrich, St Louis, USA) for coating bath preparation.

For chemical pretreatments, commercial SurTec® products (SurTec International GmbH, Bensheim, Germany; supplied by SurTec Adria d.o.o., Ljubljana) were employed: (i) SurTec® 089, a detergent booster with non-ionic surfactant alcohols (ethoxylated amines, alkyls, and fatty alcohols), (ii) SurTec® 132, a slightly alkaline builder (tetrapotassium pyrophosphate-based, silicate-free), (iii) SurTec® 496, a high-end desmutting agent comprising H_2SO_4, Fe(III) salts, HNO_3, and HF.

All aqueous solutions were prepared using Milli-Q Direct ultrapure water (Millipore, Billerica, MA, USA) with resistivity $\geqslant$18.2 M Ω cm at 25 °C and total organic carbon <5 ppb, used for both rinsing and solution preparation.

2.2.1. Chemical surface pretreatment

Chemical pretreatment consisted of alkaline cleaning and desmutting in an acidic solution (supplement figure S1). Samples were immersed in SurTec® solutions using a C-MAG HS 7 magnetic hotplate stirrer (IKA-Werke GmbH & Co. KG, Staufen, Germany) at 150 rpm and 60 °C for alkaline cleaning and at room temperature for desmutting. The protocol was adapted from SurTec's recommendations for aluminium alloys: (i) 10 min alkaline cleaning in 3 vol.% SurTec® 132 + 0.5 vol.% SurTec® 089 (pH ≈7.4), followed by (ii) 3 min desmutting in 20 vol.% SurTec® 496 (pH ≈0.3).

After each step, samples were thoroughly rinsed twice with Milli-Q water (supplement figure S1): (i) a 30 s vigorous wash from both sides using a wash bottle, and (ii) a 1 min immersion in a clean water bath. This double rinse is essential since ZrCCs are extremely sensitive to alkaline carry-over. Effective surface cleaning was verified by the water-break test, in which the surface remained uniformly wetted after rinsing (an indicator of complete contaminant removal and hydrophilicity). Note that as-received refers to samples without any mechanical treatment, regardless of whether they were chemically pretreated or further converted.

2.2.2. Zirconium conversion treatment

Immediately after pretreatment, the wet samples were immersed in freshly prepared H_2ZrF_6 conversion baths.

The baths were formulated by diluting a 50 wt. % H_2ZrF_6 solution in water to 150 ppm, then adjusting the pH to ≈4.6 with 15 wt. % NH_4HCO_3. Conversion was performed in Teflon beakers (250 ml) at room temperature (22 ± 1 °C) for 230 s (3 min 50 s), as described in the [31]. Samples were suspended vertically and gently moved during immersion to ensure uniform wetting. After treatment, each specimen was (i) rinsed twice with Milli-Q water (30 s vigorous + 30 s immersion) and (ii) dried with compressed N_2 from bottom to top, followed by 10 min of air drying at 80 °C on a C-MAG HP 4 hotplate. The three-step zirconium conversion coating process is schematically presented in figure 1(d).

Commercial SurTec® cleaners were intentionally used to ensure standardised, reproducible cleaning and desmutting conditions, thereby avoiding the variability inherent to laboratory-prepared solutions.

Thus, the focus of this study is rather the development of an in-house H_2ZrF_6 conversion bath, enabling a systematic investigation of coating deposition on aluminium heat exchangers for commercial applications.

2.3. Surface characterisation techniques

2.3.1. Scanning electron microscopy (SEM)

SEM characterisation was performed on smaller cut pieces (1–2 cm^2) and examined either in the as-received state or after surface preparation (coated with ZrCC). Before analysis, the samples were coated with a thin carbon layer using a BAL-TEC SCD 005 coater to prevent charging of the sample surface. Surface morphology was examined by Thermo Fisher Verios 4 G HP operated at 2–10 kV with secondary electrons (SEs) using the Everhart–Thornley detector (ETD), the through-the-lens detector (TLD), and a concentric back-scatter detector (CBS). Elemental compositions were determined by energy-dispersive x-ray spectroscopy (EDS) using an AZtec Live, Ultim Max SDD 65 mm^2 on selected areas (marked with *x* in the images), with a 2 μm^2 analysis area.

The cross-section of the lamella preparation for scanning transmission electron microscopy (STEM) analysis was performed using a focused ion beam/scanning electron microscope (FEI Helios NanoLab 600 Dual-beam). Imaging was carried out in SE mode using an ion conversion and electron detector at an acceleration voltage of 10 kV. The produced specimen was further analysed by applying a STEM mode of operation (Thermo Fisher Verios 4 G HP) and using a high-angle annular dark-field (HAADF) detector at 15 kV.

2.3.2. x-ray photoelectron spectroscopy (XPS)

XPS analyses were conducted using a PHI Genesis spectrometer (Physical Electronics, USA) with a monochromatic Al Kα source ($h\nu$ = 1486.6 eV, 15 kV, 100 μA). Survey spectra were collected over 0–1100 eV (pass 280 eV, step 0.5 eV), and high-resolution scans for C 1s, O 1s, Al 2p (55 eV pass, 0.1 eV step), and Si 2p, Fe $2p_{3/2}$, Zr 3d, F 1s (140 eV pass, 0.25 eV step) were acquired.

Atomic percentages for C, O, F, Al, Si, Fe, and Zr were determined from the survey spectra using standard relative sensitivity factors (RSFs) based on the Scofield cross-sections and instrument transmission function. After Shirley's background subtraction, the integrated peak areas of the C 1s, O 1s, F 1s, Al 2p, Si 2p, Fe $2p_{3/2}$ and Zr 3d signals were corrected using the RSFs supplied by the instrument database. The resulting values were normalised to 100 at.% to obtain the elemental composition of the outermost ∼5 nm of the surface. Charge compensation was applied during acquisition, and all spectra were referenced to the adventitious C–C/C–H component at 284.8 eV, which served as the internal energy standard. Because no peak fitting was performed, all atomic percentages represent semi-quantitative survey-level compositions but are entirely suitable for comparing relative changes in surface chemistry during pretreatment and coating formation.

Before analysis, the sample surface was sputtered with a 1 kV Ar^+ ion beam for 1 min over a 3 × 3 mm^2 area to remove adventitious carbon. This controlled sputtering reduced the C 1s signal to approximately one-third of its initial intensity while avoiding penetration through the native oxide and preserving the integrity of the conversion coating.

2.3.3. Electrochemical measurements

Electrochemical testing was carried out using a Multi Autolab/M204 potentiostat–galvanostat (Metrohm Autolab, Netherlands) controlled by Nova 2.1.8. software.

A three-electrode configuration was used in a 250 ml corrosion cell. The samples were mounted in the cell using a dedicated holder, exposing a 1 cm^2 surface area that served as the working electrode. A

saturated silver/silver chloride electrode (Ag/AgCl; $E = 0.197$ V vs standard hydrogen electrode SHE) was used as the reference electrode, while a 5 cm long graphite rod with a 5 mm in diameter functioned as the counter electrode.

Measurements were performed in 0.1 M NaCl at room temperature (22 ± 1 °C). Samples were stabilised for 1 h at open-circuit potential (OCP) before polarisation.

Potentiodynamic polarisation curves were recorded from −250 mV vs OCP to +1 V vs Ag/AgCl at 1 mV s^{-1} [32]. Electrochemical corrosion parameters, including the corrosion current density (j_{corr}) and corrosion potential (E_{corr}), were determined from the polarisation curves using Tafel extrapolation. The breakdown potential (E_{bd}) was identified as the potential within the passive region where the current density increased sharply. The span in E_{bd} and E_{corr} was calculated as the absolute value of the difference between ($\Delta E = |E_{bd} - E_{corr}|$).

2.3.4. Neutral salt spray (NSS) testing

Accelerated corrosion testing was performed on heat-exchanger material, cut into approximately 10 cm × 6 cm samples (marked area in the square in figures 1(a) and (b)). NSS exposure was conducted in accordance with ASTM B117-19 [33] in a controlled salt-fog chamber (HKT 750 BASIC-LINE, Köhler Automobiltechnik GmbH, Germany; chamber volume 0.750 m^3). The corrosive medium consisted of a 50 ± 1 g l^{-1} NaCl solution. Its pH was adjusted to 6.0–6.5 at room temperature (22 ± 1 °C) and stabilised at 6.5–7.2 once the solution reached the operating temperature of 35 ± 2 °C. pH adjustments were performed using 0.1 M NaOH or HCl.

Salt solution was pressurised and filtered through a filtration system to remove particulates and oil residues. The air stream was humidified before entering the spray nozzle to ensure stable fog formation, functionally equivalent to the humidification tower employed in comparable NSS systems. Spray deposition was monitored using standardised collectors consisting of a 100 mm-diameter funnel (collection area ≈80 cm^2) connected to graduated cylinders. The deposition rate was regulated to approximately 1 ml h^{-1} throughout the test.

As-received and Zr-coated specimens were mounted on chamber racks at an inclination designed to ensure uniform exposure; in accordance with ASTM recommendations and consistent with comparable studies, the samples were positioned at 45°. The total exposure duration was 90 h. At predetermined intervals, specimens were removed from the chamber, rinsed with distilled water, and dried using nitrogen gas. Surface evaluation was documented photographically before testing (0 h) and after testing (12 h, 60 h and 90 h). A long-term immersion test was monitored at 168 (1 week) and 336 h (2 weeks), supplement figures S6(b) and S7(b).

3. Results and discussion

3.1. SEM/EDS characterisation of as-received and ZrCC-coated surface

Surface morphology and chemical composition of as-received and zirconium conversion-coated tube and fin substrates were investigated by SEM/EDS, figures 2–5. Quantitative atomic concentrations extracted from EDS spectra are reported in weight percent (wt.%) in the corresponding SEM micrographs at the marked areas (x). The SEM technique identified surface features and the distribution of IMPs, which can influence (i) corrosion at local sides and (ii) ZrCC nucleation and growth.

3.1.1. As-received tube

The surface of the as-received tube material exhibits a pronounced rough morphology characterised by longitudinal valleys, grooves, and scratches (figure 2). This surface topography results from the extrusion-based manufacturing process [5]. Extrusion is usually performed at 450 °C–470 °C and 40–50 MPa. This process increases roughness and effective surface area and introduces local geometric shielding effects, thereby impairing the uniformity. The passive film is formed at high temperatures, which affects film formation and the stability of the native aluminium oxide film. As a consequence, surface passivation becomes locally less effective, thereby enhancing susceptibility to localised corrosion initiation in chloride-containing environments [5].

Back-scattered electron (BSE) imaging (CBS detector) displays strong atomic-number contrast (darker: lighter elements; brighter: heavier elements) and reveals elongated intermetallics ranging from a few hundred nanometres to 1 μm in size (figure 2(a)). EDS analysis at area x_1 indicates that the matrix is mainly aluminium (98.6 wt. %), with a low oxygen content (1.4 wt. %), consistent with pure aluminium with a thin, native oxide film formed after extrusion and storage at ambient conditions [3, 34, 35]. In contrast, in figure 2(b), the bright features correspond to Fe-rich intermetallic phases (area x_2)

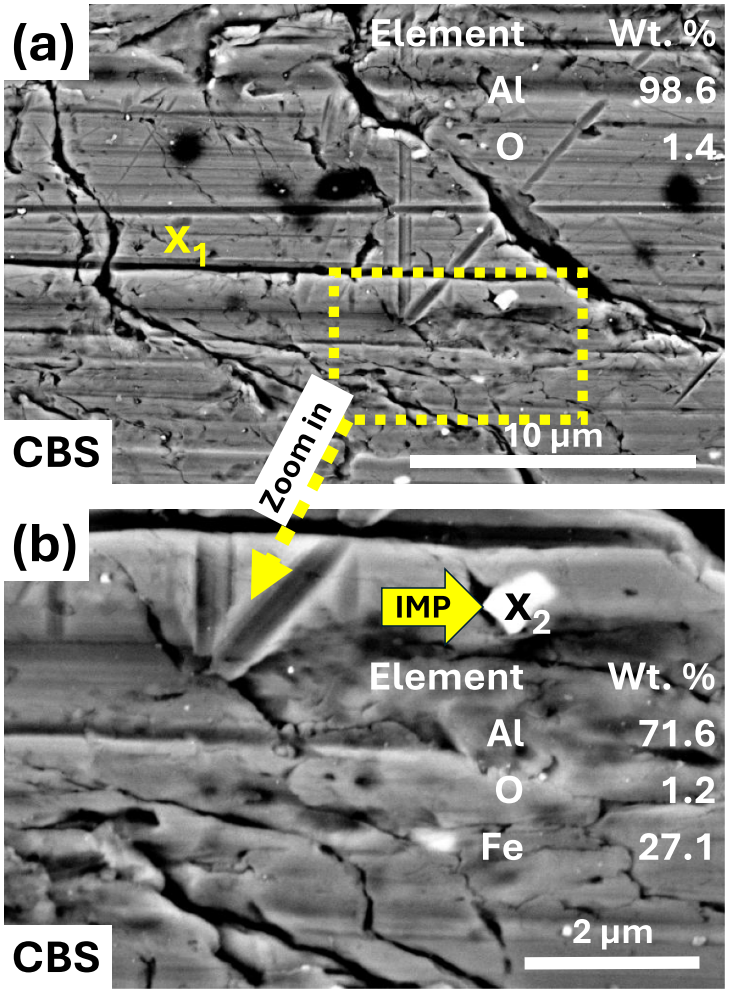

Figure 2. Back-scattered SEM image of (a) the tube and (b) an enlarged view of the selected region. The positions marked x_1 and x_2 indicate the locations where EDS analyses were performed. The corresponding elemental compositions are given as weight percentages (wt. %).

with 27.1 wt. % of Fe, which are common impurity-related constituents of wrought aluminium (1xxx-series) [3, 4].

These Fe-rich IMPs are electrochemically nobler than the surrounding aluminium matrix and therefore act as local cathodes, while the aluminium matrix behaves as an anode [36, 37]. The resulting microgalvanic coupling leads to localised cathodic oxygen reduction at the IMPs and enhanced anodic dissolution of the aluminium matrix during immersion in NaCl solution.

The extrusion-induced surface roughness and the distribution of Fe-rich intermetallics jointly control the corrosion behaviour of the as-received tubes. They are also important for the heterogeneous nucleation and growth of ZrCCs by influencing local electrochemical reactions and pH gradients at the metal–solution interface; more specifically, as detailed in section 3.1.3 [19].

3.1.2. As-received fin

In contrast to the tube, the as-received fin material exhibits a smoother, more uniform surface with fewer valleys (figure 3, supplement figure S2) and shallower marks at the sheet surface, both resulting from cold-rolling and subsequent fin-forming operations. Unlike the extrusion-induced morphology of the tube, these features are more uniformly distributed (even small Fe-IMPs are more commonly seen and are better detected under the microscope on the fins than on the tube surface), reflecting the lower degree of plastic strain imposed during fin manufacturing. A smoother surface usually promotes a more continuous native oxide film, although local compositional and microstructural heterogeneity remains evident in the CBS image in Fe-rich IMPs are again observed as bright regions within the aluminium matrix (figure 3(a)).

In addition, figure 3(b) (supplement figure S2), a SE image (using a TLD detector) at higher magnification, shows that the aluminium surface exhibits a microstructured morphology, indicative of the

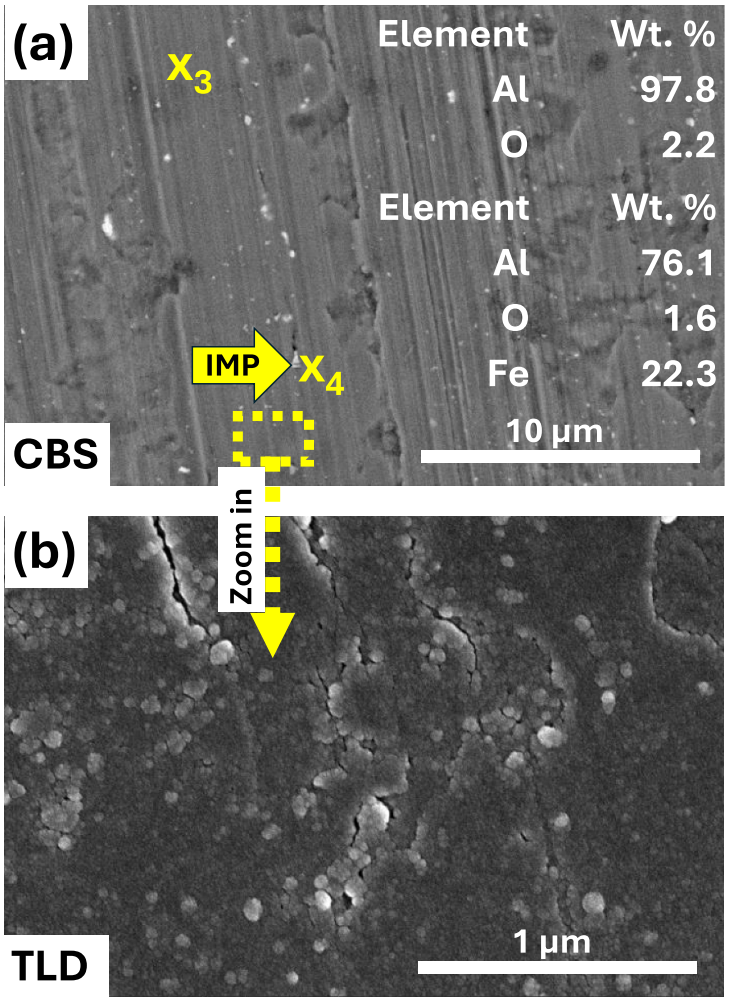

Figure 3. (a) Back-scattered SEM image of the fin and (b) secondary electron SEM image of an enlarged view of the selected region. The positions marked x_3 and x_4 indicate the locations where EDS analyses were performed. The corresponding elemental compositions are given as weight percentages (wt. %).

formation of a thin, naturally passivating oxide layer during the cold-rolling. Due to formation at ambient temperatures (much lower than those on coils), its oxide film is more discontinuous, as evidenced by microcracks and surface defects. Such discontinuities arise from local variations in oxide growth, residual stresses, and underlying microstructural heterogeneity. The cracked regions locally expose the aluminium substrate, thereby facilitating corrosion upon exposure to a corrosive medium. Although the fin surface exhibits lower topographical roughness than the tube, its thin gauge and large exposed surface area render it more susceptible to localised corrosion, underscoring its critical role in heat-exchanger degradation.

EDS data indicate a comparable chemical composition of the aluminium matrix (area x_3) to that of the tube (aluminium and a small amount of oxygen), and brighter areas related to IMPs with a large amount of iron (area x_4, 22.3 wt. %), confirming that both components are based on low-alloyed aluminium containing Fe-rich IMPs. Nevertheless, the fin surface appears less matrix-dominated in the analysed regions, with more spectra exhibiting strong Fe enrichment. Although these IMPs are expected to act as local cathodes, their altered morphology and distribution suggest a greater microgalvanic contrast than in the tube. Such differences are relevant not only for corrosion initiation but also for subsequent ZrCC nucleation behaviour.

3.1.3. ZrCC-coated tube

After a 3-step surface treatment to deposit a zirconium conversion coating, the tube surface is covered by a nanoceramic protective layer (figure 4). In figure 4(a), CBS SEM observations reveal a non-uniform distribution of Zr-rich regions (several random bright spots/areas), with preferential deposition at Fe IMPs (one of them marked with arrows).

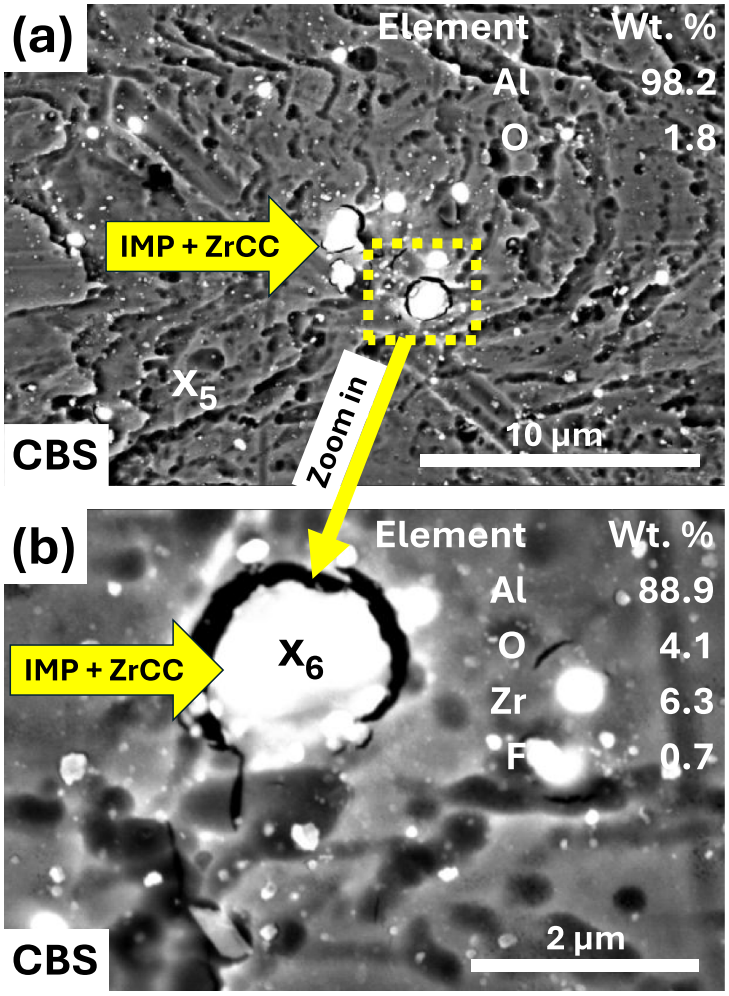

Figure 4. Back-scattered SEM images of (a) the tube coated with a ZrCC and (b) an enlarged view of the selected region. The positions marked x_5 and x_6 indicate the locations where EDS analyses were performed. The corresponding elemental compositions are given as weight percentages (wt. %).

Figure 4(b) shows a high-magnification BSE SEM image of a Fe-rich IMP covered by a ZrCC. A pronounced Zr-enriched region is observed at the IMP surface, confirming preferential ZrCC deposition at cathodic intermetallic sites.

This selective deposition of $ZrO_2/Zr(OH)_4$ is consistent with the accepted mechanism of ZrCC formation [19, 21–23], in which cathodic IMPs enhance local oxygen reduction reactions, thereby increasing interfacial pH and accelerating the hydrolysis and precipitation of zirconium-containing species [31, 38–40].

In addition, the crack is clearly visible at the periphery of the coated IMPs. This cracking is attributed to (i) surface pretreatment before ZrCC deposition [19, 21–23], and (ii) local stress development within the conversion layer, arising from preferential coating thickening at the IMP, differences in volume expansion between the hydrated ZrCC and the substrate [19, 21–23]. Such cracks are frequently reported for ZrCCs formed at the cathodic sites with high cathodic overpotential and do not necessarily indicate coating delamination; rather, they reflect localised growth-induced stresses in regions of intensified deposition.

Due to the rough surface and nanometric thickness of the ZrCC layer, EDS analyses of the aluminium matrix at area x_5 did not detect the ZrCC coating, as this technique is not suitable for analysing nanometric layers at 10 kV due to its high analysis depth. On the other hand, the area x_6 shows the presence of Zr and F, and a higher amount of O (4.1 wt. % with coating compared to 1.2 wt. % without it). The 6.3 wt. % of Zr, and 0.7 wt. % of F are suggested typical compositions, which include approximately 6–7 wt. % Zr, 3–5 wt. % O, and around 1 wt. % F [19, 21, 22, 38]. The high residual Al signal indicates that the conversion coating thickness remains well within the EDS interaction volume, as expected for thin layers. The detection of fluorine reflects partial incorporation or adsorption of fluoride species originating from the fluoro-zirconate precursor during coating formation. The observed lateral

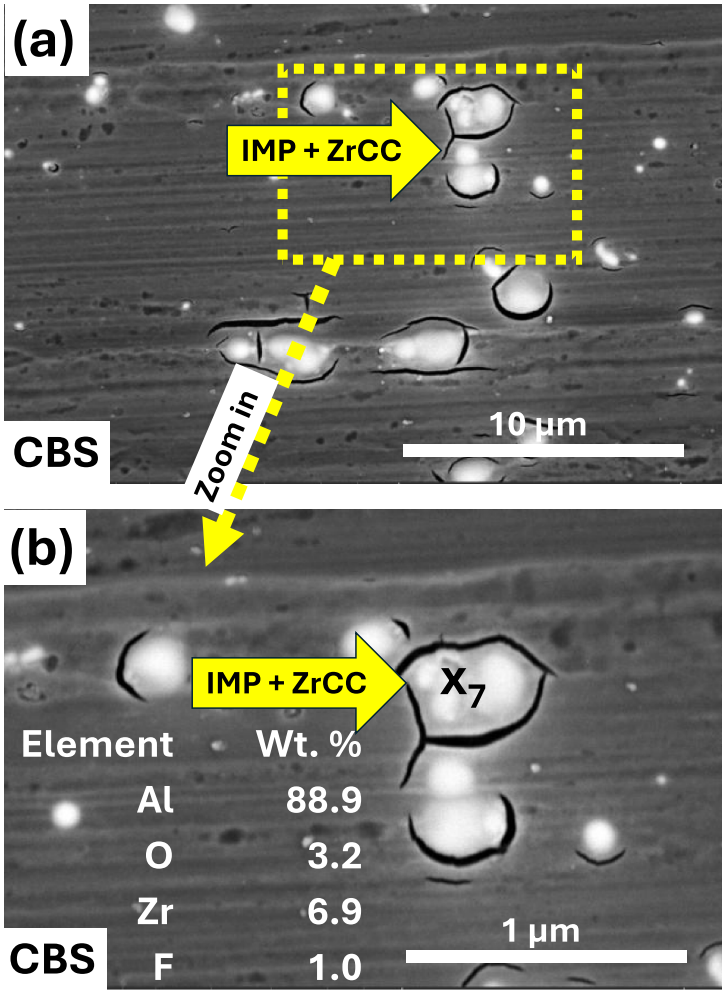

Figure 5. Back-scattered SEM images (a) of the fin coated with a ZrCC and (b) secondary electron imaging of an enlarged view of the selected region. The position marked x_7 indicates the locations where EDS analyses were performed. The corresponding elemental compositions are given as weight percentages (wt. %).

heterogeneity in Zr distribution closely follows the spatial arrangement of IMPs and extrusion-induced surface features, highlighting the dominant role of substrate microstructure in governing local coating growth kinetics.

3.1.4. ZrCC-coated fin

The ZrCC formed on the fin surface is more compact than that on the tube surface, due to the smoother surface (figure 5(a)). The step-by-step analysis of chemical pretreatment, including (i) alkaline cleaning and (ii) desmutting, reflects changes of surface topography, especially after acidic desmutting (supplement figure S2), where the native oxide film is removed, and IMPs become more pronounced at the aluminium surface [17, 18].

The final coated surface exhibits a morphology characteristic of a thin ZrCC on an aluminium matrix, with micrometre-scale thickness at the intermetallic. The deposition is again mainly observed in the Fe-rich IMPs, where a locally intensified cathodic activity promotes increased ZrCC growth (figure 5(a), marked with arrows). In the SEM image using the CBS detector in figure 5(a) (supplement figure S2, TLD detector), microcracks are again observed near larger IMPs, likely for the same reasons as in the tube: surface pretreatment before ZrCC deposition, locally thicker coating regions, and associated growth-induced stresses.

EDS results show Zr contents of 6.9 wt. %, 1 wt. % F and 3.2 wt. % O levels comparable to those measured on the coated tube (figure 4). Notably, the fin exhibits a slightly higher Zr surface concentration and more pronounced Zr enrichment around IMPs. This behaviour is likely related to the fin's thinner gauge, rolling-induced microstructural heterogeneity, and a surface state that appears more uniformly activated following pretreatment. Despite local variations in thickness and composition, the coating is adherent and continuous, with no evidence of delamination.

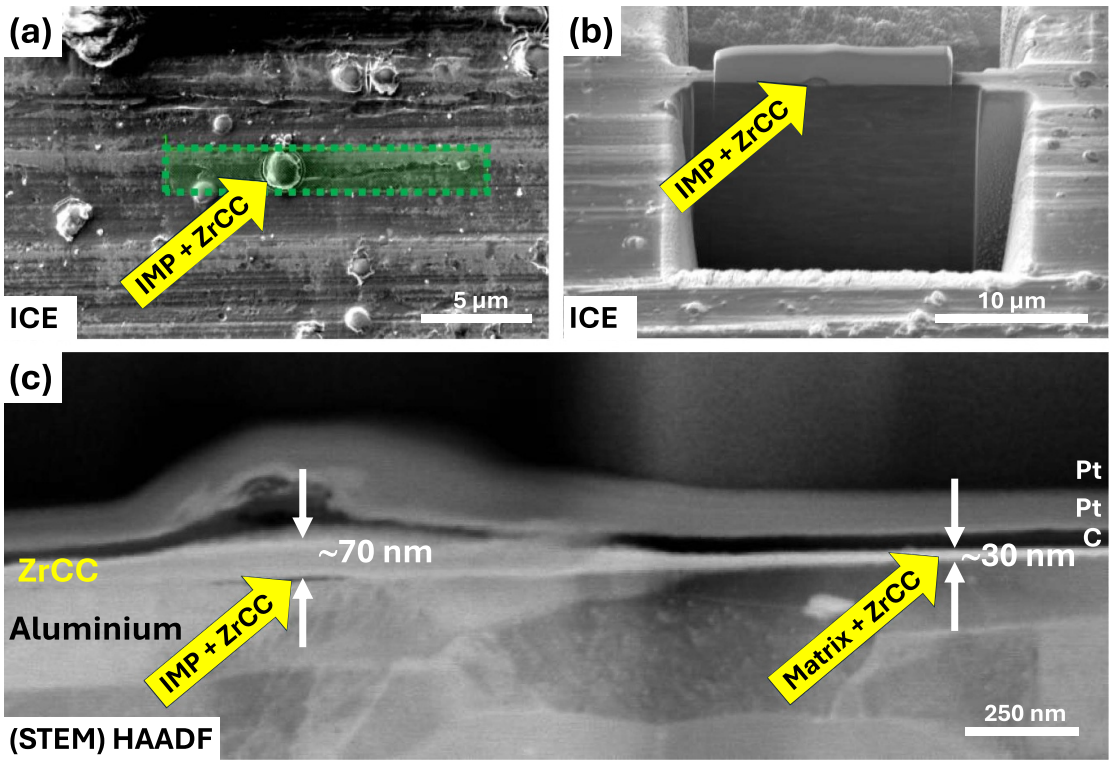

Figure 6. (a) Surface appearance of the fin coated with a ZrCC; the green dashed rectangle indicates the analysed area containing intermetallic particles covered by ZrCC (IMP + ZrCC). (b) FIB-milled trench prepared at the selected location for cross-sectional analysis. (c) Cross-sectional HAADF-STEM image of the ZrCC formed on aluminium. The ZrCC layer is visible above the aluminium substrate, with local coating thicknesses indicated for regions above intermetallic particles (IMP + ZrCC) and the aluminium matrix (matrix + ZrCC).

Further ZrCC coating characterisation at the matrix and at the IMP was performed using a cross-sectional analysis of the fin by FIB-SEM (figures 6(a) and (b)). The cross-sectional image (figure 6(c)) reveals that a Zr-based conversion coating was deposited on the matrix and preferentially on the IMP, with thicknesses ranging from ∼30 to 70 nm. The thicker ZrCC coating was observed at IMPs, confirming that coating growth is predominantly substrate-controlled by cathodic IMPs rather than laterally uniform at the aluminium surface.

The surface morphologies, compositional trends, and thickness variations observed for both fin and tube substrates are in good agreement with literature reports on zirconium-based conversion coatings on other series of aluminium alloys [31, 38–40]. The results confirmed that ZrCC formation is strongly governed by substrate microstructure, particularly the presence, morphology, and distribution of Fe-rich IMPs.

3.2. XPS characterisation of as-received and ZrCC-coated surface

XPS analysis was performed to characterise the aluminium surfaces in the (i) as-received state and (ii) after ZrCC deposition.

Survey spectra (supplement figure S3) confirm the successful formation of zirconium-based conversion coatings on both tube and fin components treated with H_2ZrF_6. Oxygen is the dominant surface element (∼55 at.%), consistent with the mixed oxide–hydroxide character of ZrCCs widely reported for aluminium alloys [41, 42]. After conversion treatment, pronounced attenuation of the metallic Al 2p signal, together with the appearance of Zr and F demonstrates effective coverage of the substrate by a Zr-rich layer. The extent of Al suppression is comparable to that previously reported for aluminium 1xxx substrates treated under similar conditions [43].

Signals from Fe and Si originate from Al–Fe–Si IMPs exposed during alkaline cleaning and desmutting (supplement tables S1 and S2). While EDS does not detect Si due to its limited lateral and depth resolution, XPS, owing to its superior surface sensitivity, clearly reveals Si associated with these near-surface intermetallics [38].

Table 1. Surface elemental composition (at. %) of as-received and ZrCC-coated tube, determined from XPS survey spectra.

Tube	C 1s	O 1s	F 1s	Al 2p	Si 2p	Fe $2p_{3/2}$	Zr 3d
As-received	38.2	41.8	—	18.3	1.7	0.1	—
ZrCC-coated	34.3	44.9	4.8	6.5	0.7	0.7	8.2

Table 2. Surface elemental composition (at. %) of as-received and ZrCC-coated fin, determined from XPS survey spectra.

Fin	C 1s	O 1s	F 1s	Al 2p	Si 2p	Fe $2p_{3/2}$	Zr 3d
As-received	59.1	33.5	—	7.2	0.3	0.0	—
ZrCC-coated	25.6	49.2	6.3	2.0	0.0	0.4	16.6

Namely, in the as-received condition (tables 1 and 2), the tube exhibits a higher detectable Si content than the fin (1.7 vs 0.3 at.%). However, this apparent difference coincides with substantially higher carbon coverage on the fin surface (59.1 vs 38.2 at.%), which attenuates substrate-derived signals within the XPS information depth. After alkaline cleaning and desmutting (supplement tables S1 and S2), carbon is significantly reduced, and the Si levels on both substrates converge to comparable values (∼2 at.%), demonstrating that the initially low Si signal on the fin was primarily due to surface contamination rather than intrinsic compositional differences.

High-resolution spectra of C 1s, O 1s, Al 2p, Si 2p, Fe $2p_{3/2}$, and F 1s are shown in supplement figures S4 and S5. Changes in Fe $2p_{3/2}$ and F 1s after pretreatment reflect the removal of the native aluminium oxide film and increased exposure of Fe-rich intermetallic sites, consistent with SEM observations (supplement figure S2). The presence of fluorine originates from the desmutting solution, where HF promotes strong Al–F complexation and matrix dissolution, facilitating particle dropout of second-phase constituents and removal of residual grinding debris [40, 44–46].

A key distinction emerges after desmutting: the fin exhibits markedly stronger Fe enrichment (1.0 at.% vs 0.1 at.% on the tube; supplement tables S1 and S2), indicating more extensive exposure of Fe-containing Al–Fe–Si IMPs due to preferential dissolution of the surrounding aluminium matrix. These sites are known to act as cathodic centres, influencing local electrochemical activity during subsequent conversion treatment.

The Zr 3d, O 1s, and F 1s spectra of the coated surfaces (figures 7 and 8) confirm the formation of a hydrated zirconia layer. The Zr $3d_{5/2}$ component at 182.1–182.4 eV with the characteristic doublet separation corresponds to Zr(IV) in $ZrO_2/Zr(OH)_4$ [47, 48]. The O 1s peak comprises contributions at ∼530.5 eV and ∼531.7 eV, assigned to oxide and hydroxyl species, confirming the hydrated nature of the conversion layer. Fluorine incorporation is evidenced by the F 1s signal at ∼684.8 eV, attributed to Zr–F and Al–F species formed through partial hydrolysis of fluoro-zirconate complexes and precipitation of zirconium hydro(oxy)fluoride intermediates [38]. These chemical signatures are fully consistent with the established ZrCC formation mechanism involving fluoride-assisted dissolution of the native Al_2O_3 film and intermetallics, followed by hydrolysis of Zr–F complexes and precipitation of hydrated zirconia species [17, 19, 49, 50].

Quantitative compositions after conversion are summarised in tables 1 and 2, with pretreatment-stage evolution provided in supplement tables S1 and S2.

For the tube samples, Zr reaches 8.2 at.% after conversion, accompanied by a strong suppression of the Al 2p signal (6.5 at.%). A residual Si signal (0.7 at.%) remains detectable, indicating that within the XPS sampling depth, some substrate-derived contributions persist, suggesting locally thinner regions or less complete coverage.

In contrast, the coated fin develops a markedly more Zr-rich surface. Zr increases to 16.6 at.% (twice that measured on the tube) while the Al 2p signal is nearly completely suppressed (2.0 at.%). Importantly, the Si signal decreases below the detection limit. Considering that both substrates exhibited comparable Si levels (∼2 at.%) immediately before conversion (supplement tables S1 and S2), the stronger attenuation of substrate-derived Al and complete suppression of Si on the fin indicate formation of a thicker and/or more continuous Zr-rich conversion layer within the XPS sampling depth. The higher Zr incorporation on the fin can be rationalised by substrate-dependent differences in intermetallic exposure after desmutting. The stronger Fe enrichment on the fin surface indicates a higher density of cathodically active Al–Fe–Si intermetallic sites. During immersion in the H_2ZrF_6 bath, these sites promote local alkalisation, accelerating hydrolysis of fluoro-zirconate complexes and enhancing Zr

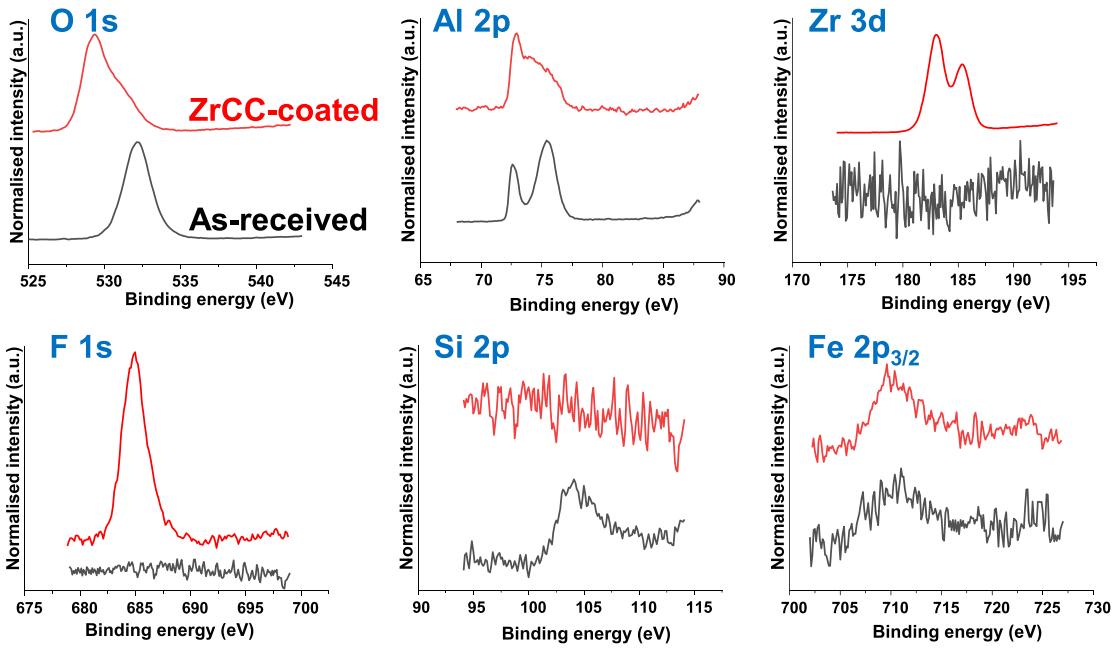

Figure 7. High-resolution XPS spectra of tube samples without (black curves) and with ZrCC (red curves): O 1s, Al 2p, Zr 3d, F 1s, Si 2p, and Fe $2p_{3/2}$ regions.

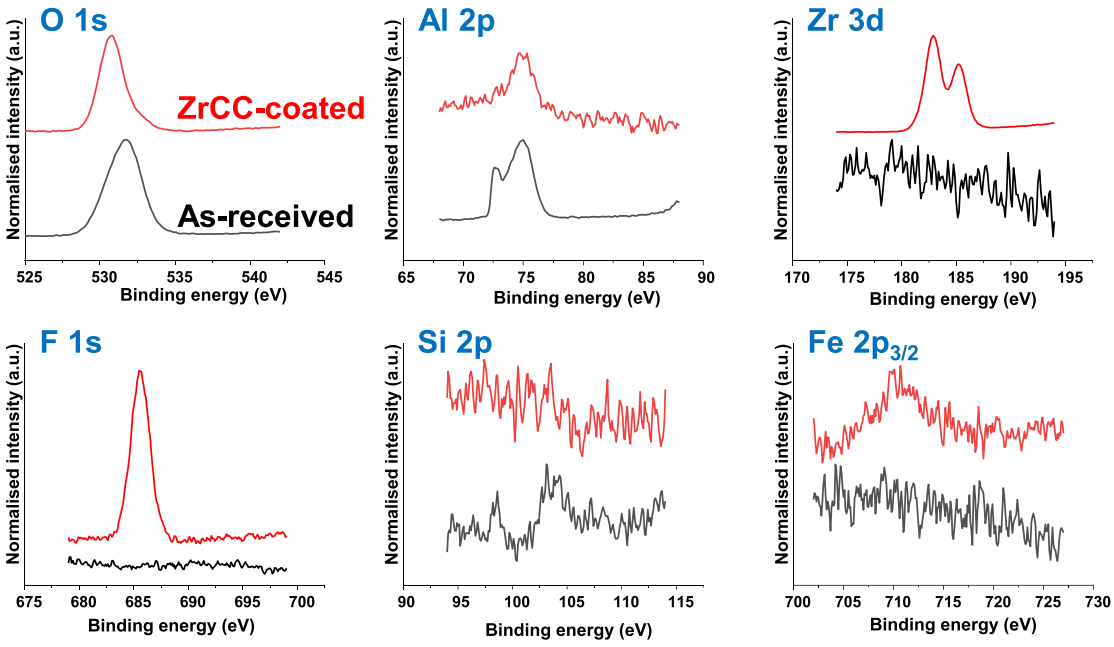

Figure 8. High-resolution XPS spectra of fin samples without (black curves) and with ZrCC (red curves): O 1s, Al 2p, Zr 3d, F 1s, Si 2p, and Fe $2p_{3/2}$ regions.

precipitation [17, 19, 49, 50]. The increased density and activity of such nucleation sites therefore facilitate more extensive lateral growth of the hydrated zirconia layer.

This mechanistic difference is directly reflected in the higher Zr content and stronger attenuation of substrate signals measured on the fin. The XPS results are in good agreement with SEM/EDS observations (figures 4–6) and previously reported correlations between Zr incorporation and improved corrosion protection of aluminium substrates [31, 38] and the references cited therein.

It is important to note that after mild Ar^+ sputtering to reduce adventitious carbon while preserving the native oxide and conversion layer, the residual C 1s signal (tables 1 and 2) with corresponding high-resolution spectra shown in supplement figures S4 and S5 reflects near-surface adsorption rather than bulk contamination. The elevated carbon levels in the as-received samples originate from industrial

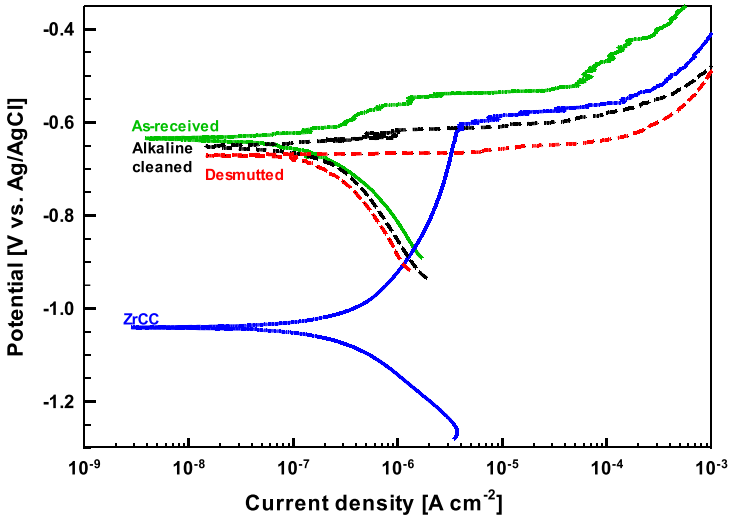

Figure 9. Potentiodynamic polarisation curves of tube samples for as-received and after alkaline cleaning, desmutting and ZrCC formation, recorded in 0.1 M NaCl.

processing and storage and are particularly pronounced on the fin (59.1 at.% vs 38.2 at.% on the tube). Alkaline cleaning and desmutting (supplement tables S1 and S2), progressively reduce carbon content, confirming effective removal of weakly bound organic residues before ZrCC deposition.

Overall, XPS confirms that both geometries develop hydrated $ZrO_2/Zr(OH)_4$ conversion layers containing fluoride species, with effective suppression of metallic aluminium and chemical signatures consistent with state-of-the-art ZrCC systems. Geometry- and microstructure-dependent differences in surface activation lead to significantly higher Zr incorporation on the fins, indicating formation of a thicker and/or more compact Zr-rich layer within the XPS sampling depth. Based on the literature [22, 31, 38, 42, 51–55], this enhanced Zr uptake provides a plausible chemical basis for the superior corrosion protection observed for the fin component, in agreement with reports linking increased Zr content to improved protective performance of aluminium substrates.

3.3. Electrochemical characterisation of As-received, chemically pretreated and ZrCC-coated samples

Representative polarisation curves for as-received, chemically pretreated (alkaline cleaning and desmutted) and ZrCC-treated tube and fin samples are shown in figures 9 and 10. The corresponding electrochemical parameters are summarised in tables 3 and 4.

The obtained electrochemical data for tube and fin substrates in different surface states provide direct insight into the importance of individual preparation steps, their corrosion susceptibility, and the protective efficiency of the ZrCC.

As-received and chemically pretreated surfaces (decreased and desmutted) exhibit behaviour characteristic of spontaneously formed aluminium oxide films. As shown in tables 3 and 4, these conditions are associated with moderate corrosion current densities ($j_{corr} \approx 10^{-7}$–10^{-6} A cm^{-2}), slight separations between corrosion and breakdown potentials ($\Delta E \approx$10–70 mV in most cases), and the absence of a stable passive region. After chemical pretreatment (figure 9), polarisation curves show a rapid increase in current density, confirming that chemical pretreatment during alkaline cleaning removes organic contaminants, and desmutting removes the native aluminium oxide film. As a result, after desmutting, a reduced corrosion protection for the tube is noticed, reflected in an increase in $j_{corr} = 2.2 \times 10^{-7}$ A cm^{-2}, without a passivation region. Similar behaviour was also noticed for fins (figure 10). The minor changes were noticed after decreasing but greater after desmutting, $j_{corr} = 4.1 \times 10^{-7}$ A cm^{-2}, and again without the passivation region (breakdown potential less than 10 mV).

In contrast, ZrCC formation markedly alters the electrochemical behaviour of both components. As evident from figures 9, 10 and tables 3, 4 the coating induces a wide passive region and a substantial positive shift in breakdown potential, with ΔE increasing to 440 mV for the tube. The tube also exhibits slightly lower corrosion current densities (table 3), despite its rougher surface. This behaviour suggests that surface roughness promotes heterogeneous nucleation and conformal growth of the ZrCC, while the extrusion-derived microstructural uniformity of the tube may limit micro-galvanic initiation sites [56], consistent with a lower extent of formation of a hydrated $ZrO_2 \times nH_2O$) conversion layer [19, 21–23].

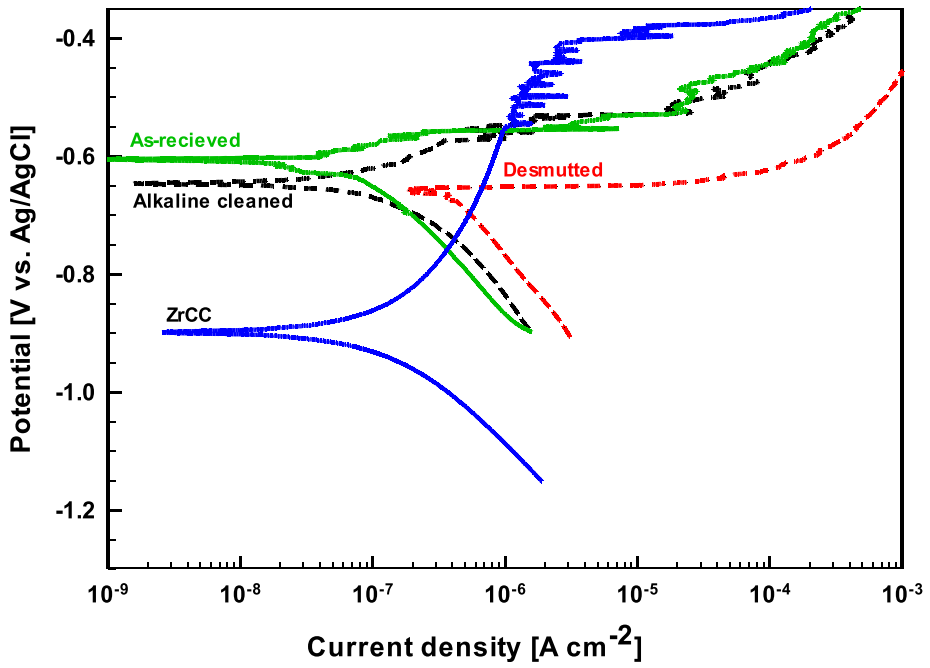

Figure 10. Potentiodynamic polarisation curves of fin samples for as-received and after alkaline cleaning, desmutting and ZrCC formation, recorded in 0.1 M NaCl.

Table 3. Electrochemical parameters for a tube sample extracted from potentiodynamic polarisation curves for as-received and after alkaline cleaning, desmutting, and ZrCC formation, recorded in 0.1 M NaCl (figure 9).

	j_{corr} (A cm^{-2})	E_{corr} (V)	E_{bd} (V)	ΔE (mV)
As-received	1.2×10^{-7}	−0.64	−0.54	100
Alkaline cleaned	1.7×10^{-7}	−0.65	−0.61	40
Desmutted	2.2×10^{-7}	−0.66	−0.65	10
ZrCC	1.7×10^{-7}	−1.04	−0.60	440

Table 4. Electrochemical parameters for a fin sample extracted from potentiodynamic polarisation curves for as-received and after alkaline cleaning, desmutting, ZrCC formation, recorded in 0.1 M NaCl (figure 10).

	j_{corr} (A cm^{-2})	E_{corr} (V)	E_{bd} (V)	ΔE (mV)
As-received	4.7×10^{-8}	−0.61	−0.56	50
Alkaline cleaned	8.5×10^{-8}	−0.64	−0.57	70
Desmutted	4.1×10^{-7}	−0.67	−0.66	10
ZrCC	7.0×10^{-8}	−0.90	−0.40	500

In contrast, the fin displays higher intrinsic reactivity in the as-received state, with less stable passive behaviour and smaller ΔE values after identical pretreatments (tables 3 and 4). This reflects its thin gauge, large exposed area, rolling-induced heterogeneity, and its deliberate role as the sacrificial component in heat-exchanger assemblies [12, , 57–59].

The greater reactivity results in a relative benefit of the ZrCC on the fin. Upon coating, the fin shows a pronounced stabilisation of the passive region and the largest increase in breakdown potential ($\Delta E \approx$500 mV; figure 10, table 4), indicating effective mitigation of surface heterogeneity and delayed pitting initiation.

Overall, while the tube retains a modest intrinsic advantage due to its geometry and microstructure, the ZrCC dominates the electrochemical response of both components and delivers functional improvements on the more corrosion-prone fin, enhancing the corrosion durability of the heat-exchanger system assembly.

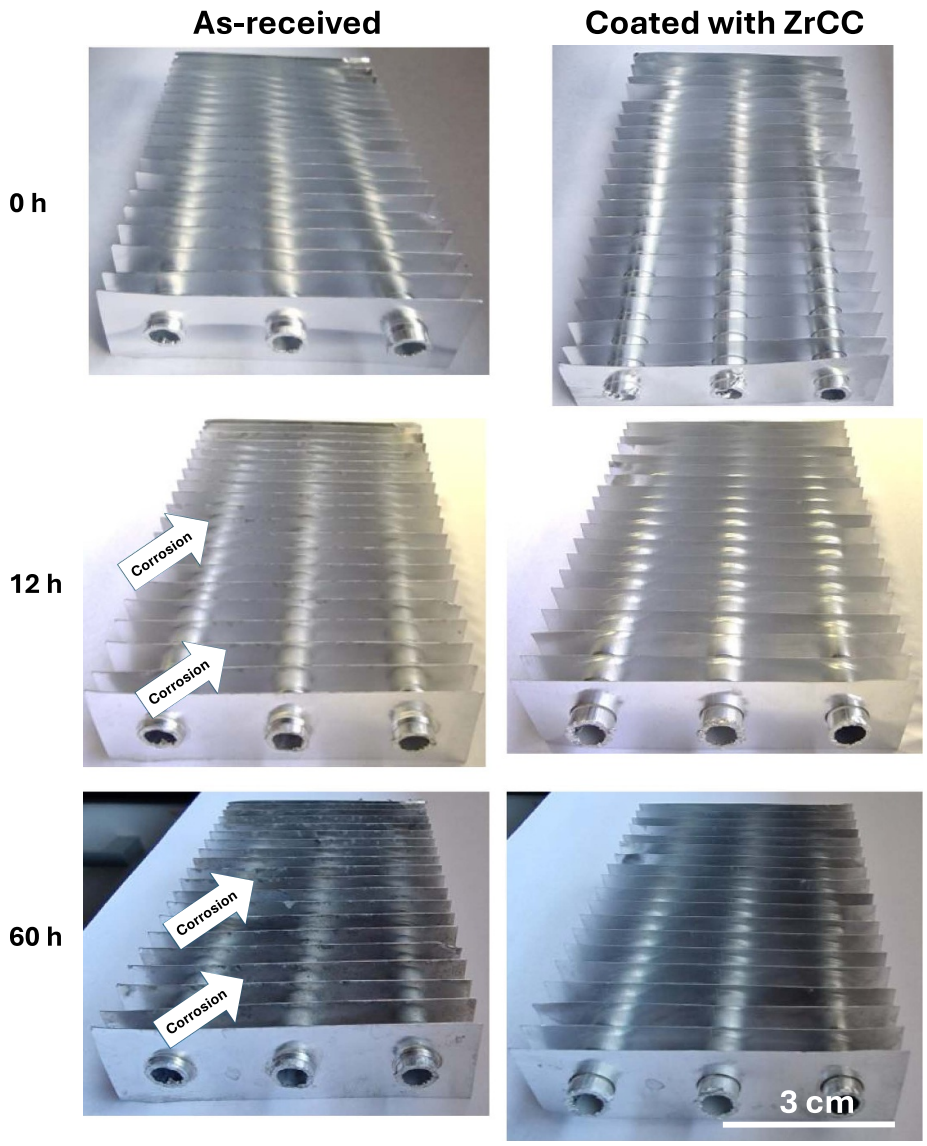

Figure 11. Surface appearance of as-received and ZrCC-coated heat exchanger (fin and tube) during neutral salt spray (NSS) exposure (after 0, 12, and 60 h) according to ASTM B117. Sample sizes were 10 cm × 6 cm.

3.4. Surface appearance during NSS testing

A salt spray test was performed to simulate the corrosion resistance of the as-received heat exchanger (galvanically coupled tubes and fins) and the surface protected with ZrCC (figures 11 and 12). Such accelerated tests represent a harsh corrosion environment (5 wt.% NaCl, 35 °C) for aluminium. Bare aluminium typically undergoes 24–72 h of ASTM B117 neutral salt spray testing for baseline comparisons, conversion coatings on this alloy last 96–168 h for industrial applications, and anodised 1050 aluminium endures 250–500 h. Therefore, the focus of the characterisation was on corrosion detection at short exposure times. In practice, bare aluminium is often used as a short-duration (24–72 h) baseline in ASTM B117 salt spray testing [33]. In contrast, conversion coatings on aluminium are commonly benchmarked over 96–168 h, with 168 h corresponding to the MIL-DTL-5541 requirement for chemical conversion coatings and anodised 1050 aluminium endures 250–500 h tested according to ASTM B117 [60].

The as-received aluminium exhibited low corrosion resistance under the test conditions: the first white, chloride-containing corrosion products (presumably $Al(OH)_2Cl$) appeared within the first 12 h and continued to spread throughout the test (figure 11). Corrosion typically starts at the edges of the fins (figure 12). The edges have lower corrosion resistance due to reduced passivation caused by cutting the plates into fins.

After 60 h (results after 90 h are shown in the supplement as figures S6(a) and S7(a)) shows that a thicker, more heterogeneous corrosion layer covered a larger surface area. In addition, a notable loss

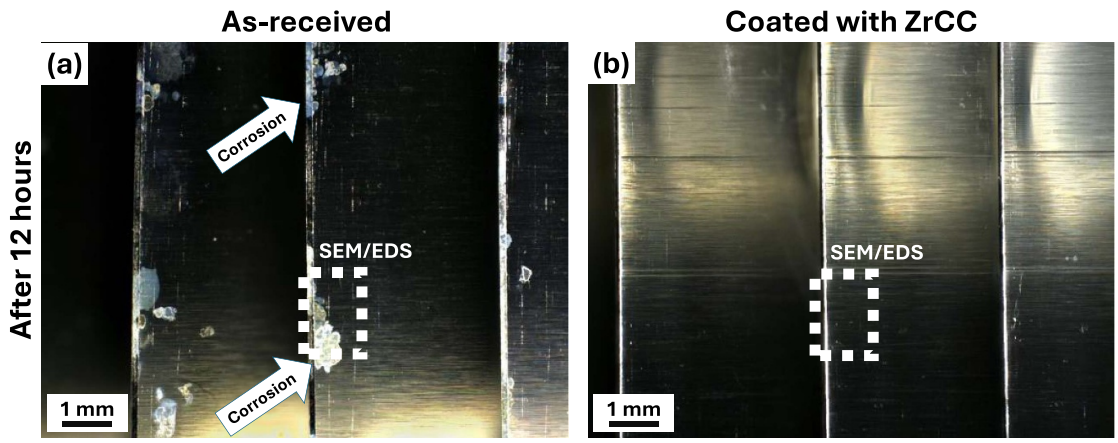

Figure 12. Surface appearance of as-received and ZrCC-coated heat exchanger (fin) during neutral salt spray (NSS) exposure (12 h) conducted according to ASTM B117.

of metallic gloss is also seen on other parts of fins and tubes. Corrosion propagated along the fins and tubes, and optical microscopy confirmed that degradation initiated at the fin edges and progressed inwards.

More initial characterisation of corrosion was performed on fins using SEM/EDS (figures 13(a) and (b)). The corrosion products are observed with the ETD detector over a large area of fins (cut area in figure 12). The CBS SEM image also revealed several small pits associated with pitting corrosion in the aluminium oxide film. The EDS data (areas x_8–x_{11}) confirmed the presence of aluminium, a great amount of oxygen (up to 20.4 wt. % at x_{11}), iron (up to 7.5 wt. % at area x_9) and some other elements as part of surface contamination (Si, Ca).

In contrast, the ZrCC-coated heat exchangers showed enhanced corrosion resistance (figure 11). Despite the ZrCC layer being only 30–70 nm thick (as determined by FIB-STEM analysis, figure 6), after 12 h of exposure, the coating provides effective corrosion protection by forming a compact barrier layer and promoting passivation; therefore, the surface showed no visible corrosion. After 60 h, only small, isolated corrosion areas were observed. Locally thicker regions at Fe-rich IMPs may enhance protection but can also lead to stress-induced cracking. The majority of the surface retained its metallic appearance, with no macroscopic coating breakdown. Microscopic examination of corrosion products along the fin edges relative to the received substrate (figure 12). The improvement is related to the border-passivation behaviour, $\Delta E = 440$ mV, figure 9, table 3. A metallic gloss is still seen on other parts of the tubes and fins. Corrosion propagated along the fins and tubes, and optical microscopy confirmed that degradation initiated at the fin edges (figure 11).

Further initial characterisation of corrosion was performed on ZrCC-coated fins after 12 and 60 h using SEM/EDS (figures 13(c) and (d)). Only a few spots of corrosion products are observed with the ETD detector, limited to a small area of fins, even at high magnification (cut area in figure 12). After 60 h, ETD and CBS SEM images also revealed several small pits. The EDS data (areas x_{12}–x_{13}) confirmed the presence of aluminium, a small amount of oxygen (up to 4.9 wt. % at x_{13}), iron (up to 0.8 wt. % at x_{13} and x_{14}) and some minor elements. The Zr content was below 0.7 wt. %, which is less than that of separately tested fins (see figure 5), but still confirms the presence of ZrCC even when the coating is deposited on a coupled tube and fin system. After 60 h, the ZrCC was not detected, but an area containing corrosion products (O up to 23.5 wt. % at x_{15}) was observed.

These results demonstrate that the ZrCC restricts the access of the chloride electrolyte to the metallic substrate and mitigates the electrochemical reactions driving aluminium corrosion. While the protection provided by thin inorganic ZrCC layers is inherently time-limited, the performance observed here is consistent with that of commercial Zr–Cr systems, which provide enhanced corrosion resistance relative to as-received aluminium in NaCl and simulated rain environments [51].

After longer exposure times (90 h, 168 h, and 336 h), corrosion further propagated on the as-received surface (supplement figures S6 and S7). The sample lost the aluminium gloss due to the formation of corrosion products at the surface.

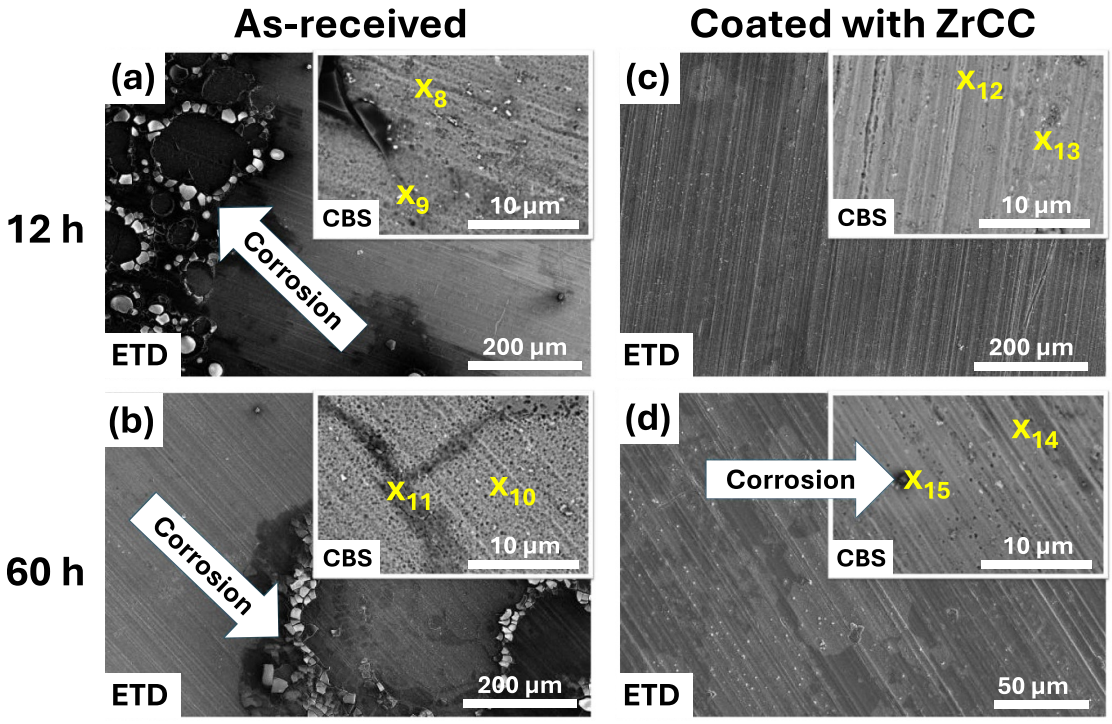

Area/elements [wt.%]	Al	O	Fe	Si	Ca	Zr
x_8	95.5	3.7	0.6		0.2	
x_9	82.8	8.5	7.5	0.4	0.8	
x_{10}	93.0	6.9	0.1			
x_{11}	79.4	20.4	0.2			
x_{12}	96.1	3.3	0.3			0.3
x_{13}	93.6	4.9	0.8			0.7
x_{14}	96.6	2.6	0.8			
x_{15}	74.5	23.5	2.0			

Figure 13. SEM images of (a), (b) as-received and (c), (d) ZrCC-coated fin specimens after 12 h and 60 h of neutral salt spray testing. Arrows indicate the locations and propagation directions of corrosion products. The regions labelled x_8–$_{15}$ denote areas where EDS corresponding elemental compositions (wt. %) are reported below the images.

After 168 h, corrosion initiation was observed on the ZrCC-coated samples with necked eye, and it became more pronounced after 336 h (supplement figures S6b and S7b). Nevertheless, even after prolonged exposure (336 h), the beneficial protective effect of the ZrCC-coated surface remained clearly evident compared with the as-received material. However, despite nanometric ZrCC layers providing time-limited protection in chloride-containing environments, the durability of the deposited ZrCC exceeds 168 h, in agreement with the expected time reported in the standard and the literature [33, 61, 62].

Overall, the present salt-spray results confirmed that ZrCC represents a viable and effective strategy for reducing corrosion activity on aluminium heat-exchanger components. Future work should focus on optimising deposition parameters, evaluating performance on larger, more complex geometries, and examining galvanic interactions in brazed assemblies, which remain critical due to their microstructural and electrochemical heterogeneities.

3.5. Discussion and ZrCC formation on heat exchanger

Although commercial aluminium contains fewer and simpler IMPs than AA5754 (alloy with Mg as a major alloying element), the general principles governing ZrCC formation remain comparable. Prior work on aluminium alloys demonstrated that Fe-containing IMPs act as local cathodes, accelerating hydroxide generation and promoting early ZrO_2 nucleation [19, 24, 25].

The formation of ZrCC on the aluminium surface proceeds through three interdependent steps [19, 23], as schematically shown in figure 14.

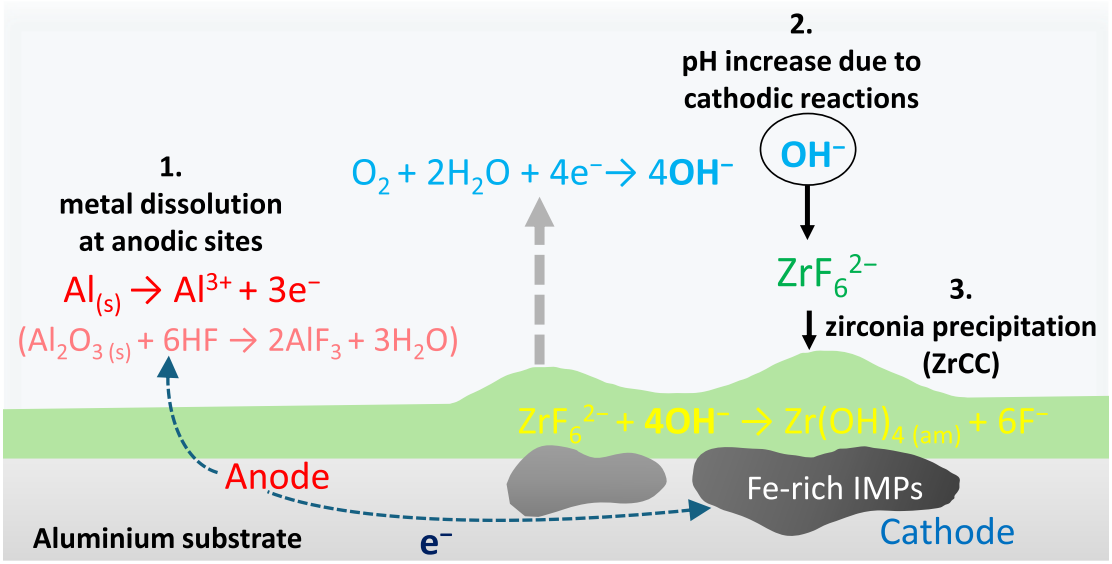

Figure 14. The scheme of three main reactions during ZrCC formation on the aluminium surface.

After chemical pretreatment (alkaline cleaning in step 1 and desmutting in the acidic solution in step 2), acidic fluoride-induced dissolution of the native oxide at the anodic sides is performed according to reaction 1:

$$Al_2O_3 + 6HF \rightarrow 2AlF_3 + 3H_2O. \quad (1)$$

At the same time, local pH elevation at IMPs due to cathodic reactions (oxygen and hydrogen reduction, reactions 2 and 3):

$$O_2 + 4H^+ + 4e^- \rightarrow 2H_2O \quad (2)$$

$$2H^+ + 2e^- \rightarrow H_2. \quad (3)$$

Due to an increase in local pH (reaction 4), hydrolysis and precipitation of zirconium (hydr)oxide from fluorozirconate species is obtained according to reaction 5:

$$O_2 + 2H_2O + 4e^- \rightarrow 4OH^- \quad (4)$$

$$ZrF_6^{2-} + 4OH^- \rightarrow Zr(OH)_4 + 6F^-. \quad (5)$$

Even though the exact IMP chemistry differs, alloys with similar cathodic-type particles [63–66] are expected to exhibit comparable ZrCC growth behaviour across the Al series [38], enabling the mechanistic understanding developed for AA5754 to be extended to commercial aluminium. As also reported for AA5754 [31, 38], surface pretreatments are crucial; specifically, alkaline cleaning of aluminium produced surfaces with reduced IMP coverage but increased IMP reactivity due to selective dissolution and partial matrix removal, in agreement with the known behaviour of HF-coating desmutting solutions [40, 45, 46]. In contrast, ZrCC-treated aluminium samples prepared under the optimised 150 ppm/230 s/pH 4.6 conditions exhibited extended passive regions and delayed pitting, reflecting suppressed cathodic activity at IMPs and the formation of a more homogeneous, crack-limited zirconia layer. Moreover, since commercial aluminium contains fewer cathodic particles than AA5754, the local pH rise during deposition is expected to be even weaker, further limiting uncontrolled polymerisation and excessive nodule growth. Based on the similar cathodic strength and behaviour of IMPs across aluminium alloys [38, 63], it is therefore reasonable that the optimal conditions determined for AA5754 are valid for another series of alloys and are also applicable to commercial aluminium.

The formed ZrCC layer contains some cracks, which are predominantly localised at Fe-rich IMPs and are attributed to growth-induced stresses in regions of preferential coating thickening. Despite cracks, electrochemical measurements reveal the formation of a wide passive region and a significant increase

in breakdown potential, indicating that the coating's overall protective effect remains dominant. In addition, the NSS results confirmed that on ZrCC-coated samples corrosion onset was significantly delayed compared to the as-received material, indicating that the coating maintains its protective function.

In light of the schematic presented reaction in the deposition mechanism, all applied characterisation techniques converge to a coherent and internally consistent description of ZrCC formation and performance on aluminium heat-exchanger components. SEM/EDS demonstrates that coating nucleation and growth are strongly substrate-controlled, with preferential deposition at Fe IMPs that act as local cathodic sites. XPS corroborates these observations by revealing compact, hydrated $ZrO_2/Zr(OH)_4$ layers incorporating residual fluoride species, with substantially higher Zr surface enrichment on fin substrates following identical processing. This enhanced Zr incorporation is reflected directly in the electrochemical response, where ZrCCs induce wide passive regions and pronounced positive shifts in breakdown potential, particularly for the intrinsically more corrosion-prone fin material.

NSS testing further validates this trend at the macroscopic scale, showing delayed corrosion initiation and limited degradation on coated samples compared with rapid attack on as-received aluminium. Collectively, these results demonstrate that zirconium conversion coatings provide efficient, geometry-independent corrosion protection while delivering their most significant relative benefit on fin components, which account for the majority of heat-exchanger failures.

4. Conclusions

This study presents the surface characterisation of aluminium heat exchangers and demonstrates that zirconium-based conversion coatings provide adequate corrosion protection for aluminium heat exchanger components. The main conclusions are:

- A compact, nanometre-thick (30–70 nm) ZrCC layer was formed through substrate-controlled nucleation on tubes and fins, preferentially depositing at Fe IMPs, which serve as locally electrochemically active sites.
- Although tube and fin substrates develop chemically similar hydrated $ZrO_2/Zr(OH)_4$ layers, fin components exhibit substantially higher zirconium incorporation following identical processing.
- The enhanced Zr enrichment translates directly into electrochemical performance, with ZrCC inducing broad passive regions and large positive shifts in breakdown potential (ΔE up to $\sim$500 mV), particularly on the intrinsically more corrosion-prone fin material.
- NSS testing confirms the practical relevance of the developed ZrCC on a heat exchanger, demonstrating delayed corrosion initiation and limited surface degradation even after 90 h of testing in NSS.
- Zirconium conversion coatings deliver geometry-independent corrosion protection while providing their greatest relative benefit on fin substrates, thereby improving heat exchangers' corrosion resistance.

These results support the implementation of optimised ZrCC as a robust pretreatment for aluminium heat exchangers and provide a mechanistic foundation for its integration into advanced industrial coating systems, particularly as an interfacial layer that enhances the adhesion and long-term performance of subsequently applied organic topcoats.

Acknowledgment

Financial support was provided by the Slovenian Research and Innovation Agency (ARIS) under the research core funding programmes P1-0134, P2-0084 and P2-0393, and through the ARIS project L2-60141 (Enhancing heat exchanger performance using advanced superhydrophobic coating; Super-COR-AI), partially co-financed by Gorenje gospodinjski aparati, d.o.o., Slovenia.

The authors also acknowledge the Center for Electron Microscopy and Microanalysis (CEMM) and Nanoscience and Nanotechnology (Nanocentre) as infrastructure units of the Jožef Stefan Institute, Slovenia, for access to the scientific equipment: a focused ion beam and a scanning electron microscope (FIB/SEM).

Data availability statement

All data that support the findings of this study are included within the article (and any supplementary files).

Supplementary data 1 available at https://doi.org/10.1088/2515-7639/ae80fe/data1.

Conflict of interest

The authors declare no conflict of interest. All authors have read and agreed to the published version of the manuscript. Data are available on request.

Author contributions

Ana Kraš 0000-0002-3499-0853
Conceptualization (equal), Data curation (equal), Formal analysis (equal), Methodology (equal), Visualization (equal), Writing – original draft (equal)

Barbara Kapun 0009-0001-3843-7588
Formal analysis (equal), Investigation (equal), Methodology (equal), Visualization (equal)

Nina Kovač 0009-0001-7729-6431
Data curation (equal), Formal analysis (equal), Methodology (equal), Visualization (equal), Writing – original draft (equal)

Matejka Podlogar 0000-0001-7892-8608
Conceptualization (equal), Formal analysis (equal), Methodology (equal), Writing – review & editing (equal)

Sašo Šturm 0000-0003-0019-7491
Conceptualization (equal), Methodology (equal), Writing – review & editing (equal)

Ingrid Milošev 0000-0002-7633-9954
Conceptualization (lead), Data curation (equal), Formal analysis (equal), Methodology (equal), Writing – original draft (equal), Writing – review & editing (equal)

Marko Kralj
Conceptualization (equal), Data curation (equal), Formal analysis (equal), Funding acquisition (equal), Project administration (equal), Resources (equal)

Peter Rodič 0000-0001-8664-0129
Conceptualization (equal), Data curation (equal), Formal analysis (equal), Funding acquisition (equal), Investigation (equal), Methodology (equal), Project administration (equal), Supervision (equal), Visualization (equal), Writing – original draft (equal), Writing – review & editing (equal)

References

[1] Ali M, Ul-hamid A, Alhems L M and Saeed A 2020 Review of common failures in heat exchangers—Part I: mechanical and elevated temperature failures *Eng. Fail. Anal.* **109** 104396
[2] Zhu H, Leng M, Jin G and Miao H 2023 A review of research on galvanic corrosion of aluminum alloys *Fluid Dyn. Mater. Process.* **19** 1907–23
[3] Sukiman NL, Zhou X, Birbilis N, Hughes AE, Mol JM, Garcia SJ, Zhou X, Thompson GE 2012 Durability and corrosion of aluminium and its alloys: overview, property space, techniques and developments *Aluminium Alloys—New Trends in Fabrication and Applications* (InTech) (https://doi.org/10.5772/53752)
[4] Zhao Q, Slagsvold M and Holmedal B 2012 Comparison of the influence of Si and Fe in 99.999% purity aluminum and in commercial-purity aluminum *Scr. Mater.* **67** 217–20
[5] Jiang R, Zhao W, Zhang L, Li X and Guan S 2023 Microstructure and corrosion resistance of commercial purity aluminum sheet manufactured by continuous casting direct rolling after ultrasonic melt pre-treatment *J. Mater. Res. Technol.* **22** 1522–32
[6] Kawahara A, Niikura A and Doko T 2003 Development of aluminum alloy fin stock for heat exchangers using twin-roll continuous casting method *Furukawa Rev.* **24** 81–87 (available at: www.furukawaelectric.com/review/fr024/fr24_16.pdf)
[7] Shang Y, Može M, Castagne S, Seveno D, Golobič I and Vetrano M R 2025 Effect of surface temperature on splashing of droplets impacting on a cold superhydrophobic surface *Appl. Therm. Eng.* **272** 126351
[8] Može M *et al* 2025 Anti-icing performance and anti-corrosive properties of superhydrophobic nanosecond-laser-textured aluminum surfaces with a self-assembled monolayer coating *Surf. Interfaces* **72** 107016

[9] Berce J, Zupančič M, Može M and Golobič I 2021 A review of crystallization fouling in heat exchangers *Processes* **9** 1356
[10] Wang Y, Zhao H and Hrnjak P 2021 An evaluation of the effect of corrosion tests on thermal performance of aluminum heat exchangers *18th Int. Refrigeration and Air Conditioning Conf.* (School of Mechanical Engineering)
[11] Lachowicz M M, Lachowicz M B and Gertruda A 2022 Assessment of the possibility of galvanic corrosion in aluminum microchannel heat exchangers *Crystals* **12** 1439
[12] Faes W, Lecompte S, Ahmed Z Y, Van Bael J, Salenbien R, Verbeken K and De Paepe M 2019 Corrosion and corrosion prevention in heat exchangers *Corros. Rev.* **37** 131–55
[13] Haomei Aluminum 2025 Aluminum fin stock (available at: www.aluminum-hm.com/application/aluminum-fin-stock/) (Accessed 13 January 2026)
[14] Pan Y, Shen Y and Zhao P 2018 The microstructure and deformation behavior of Al-Fe-Mn alloys with different Fe contents during cold rolling *Metals* **8** 753
[15] Birol F S, Birol Y and Slámová M 2002 Corrosion behavior of aluminum finstock alloys *Mater. Sci. Forum* **396–402** 1511–6
[16] Liu M, Peng H, Tao Y, Wang J and Jie G 2023 Comparative corrosion analysis of acrylic precoated aluminum foil under natural exposure and neutral salt-spray (NSS) testing *Int. J. Electrochem. Sci.* **18** 100373
[17] Andreatta F, Turco A, de Graeve I, Terryn H, de Wit J H W and Fedrizzi L 2007 SKPFM and SEM study of the deposition mechanism of Zr/Ti based pre-treatment on AA6016 aluminum alloy *Surf. Coat. Technol.* **201** 7668–85
[18] Sharifi Golru S, Attar M M and Ramezanzadeh B 2015 Effects of surface treatment of aluminium alloy 1050 on the adhesion and anticorrosion properties of the epoxy coating *Appl. Surf. Sci.* **345** 360–8
[19] Milošev I and Frankel G S 2018 Review—conversion coatings based on zirconium and/or titanium *J. Electrochem. Soc.* **165** C127–44
[20] Sattari M, Olad A, Maryami F, Ahadzadeh I and Nofouzi K 2023 Facile fabrication of durable and fluorine-free liquid infused surfaces on aluminum substrates with excellent anti-icing, anticorrosion, and antibiofouling properties *Surf. Interfaces* **38** 102860
[21] Rodič P, Kapun B and Milošev I 2024 Complementary corrosion protection of cast AlSi7Mg0.3 alloy using Zr-Cr conversion and polyacrylic/siloxane-silica multilayer coatings *npj Mater. Degrad.* **8** 58
[22] Šekularac G, Kovač J and Milošev I 2020 Prolonged protection, by zirconium conversion coatings, of AlSi7Mg0.3 aluminium alloy in chloride solution *Corros. Sci.* **169** 108615
[23] Kraš A and Milošev I 2023 The aqueous chemistry of zirconium as a basis for better understanding the formation of zirconium conversion coatings: updated thermodynamic data *J. Electrochem. Soc.* **170** 21508
[24] Golru S S, Attar M M and Ramezanzadeh B 2015 Morphological analysis and corrosion performance of zirconium based conversion coating on the aluminum alloy 1050 *J. Ind. Eng. Chem.* **24** 233–44
[25] Becker M 2019 Chromate-free chemical conversion coatings for aluminum alloys *Corros. Rev.* **37** 321–42
[26] Tomlinson C E 1995 Conversion coatings for metal surfaces *US5380374A*
[27] Siebert E J and Goodreau B H 2019 Zirconium-based coating compositions and processes *US10385219B2*
[28] Kaneko H, Ogino T and Sako R 1992 Aluminum heat exchanger coating *CA1306907C*
[29] Matsui N, Mizuno A, Wada Y, Hokke J, Nakamura K and Hirose T 2021 Surface treatment method for aluminum heat exchanger *CN108660450B*
[30] Matsui N and Okamura H 2012 Anti-corrosion treatment method for aluminum heat exchanger *US20120288634A1*
[31] Kraš A, Kramar D and Milošev I 2025 Experimental approach and assessment of Zr conversion coatings on Al alloy using response surface methodology *Corros. Sci.* **249** 112824
[32] ASTM International 2020 Test method for conducting potentiodynamic polarization resistance measurements (https://doi.org/10.1520/G0059-97R20)
[33] ASTM International 2019 Practice for operating salt spray (fog) apparatus (https://doi.org/10.1520/B0117-19)
[34] Davis G D, Moshier W C, Ahearn J S, Hough H F and Cote G O 1987 Corrosion/passivation of aluminum in dilute sulfate solutions: a comparison of Pourbaix and surface behavior diagrams *J. Vac. Sci. Technol. A* **5** 1152–7
[35] Rodič P and Milošev I 2016 Corrosion inhibition of pure aluminium and alloys AA2024-T3 and AA7075-T6 by cerium(III) and cerium(IV) salts *J. Electrochem. Soc.* **163** C85–93
[36] Milošev I, Kapun B and Rodič P 2022 The relation between the microstructure of aluminum alloy 7075-T6 and the type of cerium salt in the formation of the cerium conversion layer *J. Electrochem. Soc.* **169** 091501
[37] Rodič P, Milošev I and Frankel G S 2023 Corrosion of synthetic intermetallic compounds and AA7075-T6 in dilute Harrison's solution and inhibition by cerium(III) salts *J. Electrochem. Soc.* **170** 031503
[38] Šekularac G, Kovač J and Milošev I 2020 Comparison of the electrochemical behaviour and self-sealing of zirconium conversion coatings applied on aluminium alloys of series 1xxx to 7xxx *J. Electrochem. Soc.* **167** 111506
[39] Šekularac G and Milošev I 2020 Electrochemical behavior and self-sealing ability of zirconium conversion coating applied on aluminum alloy 3005 in 0.5 M NaCl solution *J. Electrochem. Soc.* **167** 021509
[40] Campestrini P, van Westing E P M and de Wit J H W 2001 Influence of surface preparation on performance of chromate conversion coatings on Alclad 2024 aluminium alloy: Part I: Nucleation and growth *Electrochim. Acta* **46** 2553–71 (In French)
[41] Bonamigo Moreira V, Puiggalí-Jou A, Jiménez-piqué E, Alemán C, Meneguzzi A and Armelin E 2021 Green nanocoatings based on the deposition of zirconium oxide: the role of the substrate *Materials* **14** 1043
[42] George F O, Skeldon P and Thompson G E 2012 Formation of zirconium-based conversion coatings on aluminium and Al–Cu alloys *Corros. Sci.* **65** 231–7
[43] Glover C F, Lim M L C and Scully J R 2021 Increased filiform corrosion resistance utilizing a zirconium-based conversion coating on an Al-Zn-Mg-Cu (AA7075-T6) alloy as well as selected surface treatments *Corrosion* **77** 40–52
[44] Lorking K F and Mayne J E O 1966 The corrosion of aluminium in solutions of sodium fluoride and sodium chloride *Br. Corros. J.* **1** 181–2
[45] Beck A F, Heine M A, Keir D S, van Rooyen D and Pryor M J 1962 Further studies of the electrical characteristics of oxide films on aluminium *Corros. Sci.* **2** 133–45
[46] Xue T, Cooper W C, Pascual R and Saimoto S 1991 Effect of fluoride ions on the corrosion of aluminium in sulphuric acid and zinc electrolyte *J. Appl. Electrochem.* **21** 238–46
[47] Cristaudo V, Baert K, Laha P, Lyn Lim M, Brown-Tseng E, Terryn H and Hauffman T 2021 A combined XPS/ToF-SIMS approach for the 3D compositional characterization of Zr-based conversion of galvanized steel *Appl. Surf. Sci.* **562** 150166
[48] Liu X *et al* 2019 Environmentally friendly Zr-based conversion nanocoatings for corrosion inhibition of metal surfaces evaluated by multimodal x-ray analysis *ACS Appl. Nano Mater.* **2** 1920–9

[49] Khun N W, Adhikari S, Li Y Y, Frankel G S, McGee J, Smith T, Bammel B and Zimmerman J 2017 Corrosion protection of galvanized steel by a thin hybrid coating with Zr-rich inorganic matrix and organic polymer beads *Corrosion* **73** 339–46
[50] Laha P, Schram T and Terryn H 2002 Use of spectroscopic ellipsometry to study Zr/Ti films on Al *Surf. Interface Anal.* **34** 677–80
[51] Mujdrica Kim M, Kapun B, Tiringer U, Šekularac G and Milošev I 2019 Protection of aluminum alloy 3003 in sodium chloride and simulated acid rain solutions by commercial conversion coatings containing Zr and Cr *Coatings* **9** 563
[52] Mysliu E, Sletteberg Storli K, Skogøy H M, Kubowicz S, Svenum I-H, Lunder O and Erbe A 2024 Effect of Cu2+ on deposition mechanism and structure of ZrO_2-based conversion coatings on AA6060 aluminium alloys and their susceptibility to filiform corrosion *Electrochim. Acta* **477** 143805 (In French)
[53] Cerezo J, Vandendael I, Posner R, De Wit J H W, Mol J M C and Terryn H 2016 The effect of surface pre-conditioning treatments on the local composition of Zr-based conversion coatings formed on aluminium alloys *Appl. Surf. Sci.* **366** 339–47
[54] Cerezo J, Vandendael I, Posner R, Lill K, de Wit J H W, Mol J M C and Terryn H 2013 Initiation and growth of modified Zr-based conversion coatings on multi-metal surfaces *Surf. Coat. Technol.* **236** 284–9
[55] Zhang H, Zhang X, Zhao X, Tang Y and Zuo Y 2018 Preparation of Ti–Zr-Based conversion coating on 5052 aluminum alloy, and its corrosion resistance and antifouling performance *Coatings* **8** 397
[56] Kim J-K and Park I-H 2015 Aluminum alloy composition, aluminum extrusion tube and fin material with improved corrosion durability for heat exchangers WO2015/046940A1
[57] Andreatta F, Lanzutti A and Fedrizzi L 2016 Corrosion behaviour of AA8xxx aluminium fins in heat exchangers *Surf. Interface Anal.* **48** 789–97
[58] Yu Y *et al* 2025 Failure analysis of perforation in aluminum alloy plate-fin heat exchanger for electric multiple units transformer *Eng. Fail. Anal.* **179** 109788
[59] Ifezue D and Tobins F H 2015 Corrosion failure of aluminum heat exchanger tubes *J. Fail. Anal. Prev.* **15** 541–7
[60] U.S. Department of Defense 2006 (available at: www.coastlinemetalfinishing.com/uploads/MIL-DTL-5541f.pdf) *MIL-DTL-5541F, Detail Specification: Chemical Conversion Coatings on Aluminum and Aluminum Alloys*
[61] Rodič P and Milošev I 2015 Electrochemical and salt spray testing of hybrid coatings based on Si and Zr deposited on aluminum and its alloys *J. Electrochem. Soc.* **162** C592–600
[62] Wu L, Guo R and Yin S 2022 Preparation and properties of trivalent chromium/zirconate composite conversion coating on Al-50%Si alloy *J. Phys.: Conf. Ser.* **2390** 012006
[63] Birbilis N and Buchheit R G 2008 Investigation and discussion of characteristics for intermetallic phases common to aluminum alloys as a function of solution pH *J. Electrochem. Soc.* **155** C117
[64] Jin Z, Cai C, Yuan Y, Kang D, Hunter J and Zhou X 2021 The behaviour of AA5754 and AA5052 aluminium alloys in alkaline etching solution: similarity and difference *Mater. Charact.* **171** 110768
[65] Jin Z, Cai C, Hashimoto T, Yuan Y, Kang D, Hunter J and Zhou X 2021 The behaviour of iron-containing intermetallic particles in aluminium alloys in alkaline solution *Corros. Sci.* **179** 109134
[66] Kosec T, Merl D K and Milošev I 2008 Impedance and XPS study of benzotriazole films formed on copper, copper–zinc alloys and zinc in chloride solution *Corros. Sci.* **50** 1987–97